Electromagnetic ion cyclotron wave fields in a realistic dipole field

R. E. Denton [1]

[1]Department of Physics and Astronomy, Dartmouth College, Hanover, New Hampshire, USA

Key Points:

- The latitudinal properties of electromagnetic ion cyclotron waves determine the total effect of those waves on relativistic electrons.
- The latitudinal evolution of simulated electromagnetic ion cyclotron waves is found using Fourier spectra calculated in localized regions.
- When waves propagate to high latitude, the parallel wave vector decreases, but frequency filtering can limit this effect.

Corresponding author: R. E. Denton, `redenton at dartmouth.edu`

Abstract

The latitudinal distribution and properties of electromagnetic ion cyclotron (EMIC) waves determine the total effect of those waves on relativistic electrons. Here we describe the latitudinal variation of EMIC waves simulated self consistently in a dipole magnetic field for a plasmasphere or plume-like plasma at geostationary orbit with cold cold H+, He+, and O+, and hot protons with temperature anisotropy. The waves grow as they propagate away from the magnetic equator to higher latitude while the wave vector turns outward radially and the polarization becomes linear. We calculate the detailed wave spectrum in four latitudinal ranges varying from magnetic latitude MLAT close to 0° (magnetic equator) up to 21°. The strongest waves are propagating away from the magnetic equator, but some wave power propagating toward the magnetic equator is observed due to local generation (especially close to the magnetic equator) or reflection. The He band waves, which are generated relatively high up on their dispersion surface, are able to propagate all the way to MLAT = 21°, but the H band waves experience frequency filtering, with no equatorial waves propagating to MLAT = 21° and only the higher frequency waves propagating to MLAT = 14°. The result is that the wave power averaged $k_{\|}$, which determines the relativistic electron minimum resonance energy, scales like the inverse of the local magnetic field for the He mode, whereas it is almost constant for the H mode. While the perpendicular wave vector turns outward, it broadens. These wave fields should be useful for simulations of radiation belt particle dynamics.

1 Introduction

In order to quantitatively understand relativistic electron variability, it is essential to understand both acceleration and loss mechanisms [*Summers et al.*, 2007; *Shprits et al.*, 2008]. Electromagnetic Ion Cyclotron (EMIC) waves are thought to be a major loss mechanism for relativistic electrons, especially in the dusk local time sector [*Millan and Thorne*, 2007]. *Fraser et al.* [2006] give a brief review of EMIC waves.

In quasi-linear diffusion, only electrons in resonance with the waves will be strongly affected by pitch angle scattering. A statistical study showed that most frequently the resonant energy was above 2 MeV, though it could drop to as low as 500 keV when the total density was large, such as might occur in the plasmasphere or a plasmaspheric plume [*Meredith et al.*, 2003]. But some observations suggest that significant electron precipitation may commonly occur near 300 keV [*Hendry et al.*, 2017, and references therein].

To calculate the effect of EMIC waves on relativistic electrons, it will be necessary to consider the interaction along the entire particle path, which means that it will be necessary to understand how the wave properties vary with respect to latitude. Thus it's necessary to know the distribution of wave power and polarization along magnetic field lines. It's also important to understand the variation of $k_{\|}$, the component of the wave vector parallel to the background magnetic field $\mathbf{B}$. For resonance of electrons with EMIC waves, the wave frequency (below the proton gyrofrequency), can be ignored, so the resonance condition [e.g. *Denton et al.*, 2015] is $k_{\|} v_{\|} = \Omega_{\rm ce}/\gamma$, where $v_{\|}$ is the parallel component of the electron velocity, $\Omega_{\rm ce} = eB/m_e$, e is the proton charge, m_e is the electron mass, and γ is the relativistic factor for the electron. Therefore, $k_{\|}$ is a crucial parameter determining which electrons will be in resonance with the waves.

One of the goals of this paper is to understand the variation of wave power, polarization, and $k_{\|}$ at different latitudes along the magnetic field line. In order to do this, we will use an innovative calculation of the spatial spectrum within different latitudinal ranges within the simulation. To our knowledge, such an investigation of the evolution of the spatial spectrum with respect to latitude has not previously been done. So this study can serve as a model for future investigations of the latitudinal dependence of a variety of magnetospheric waves.

To date, the EMIC wave fields used to calculate effects on relativistic particles have been found either from models [*Omura and Zhao*, 2012, 2013; *Kubota et al.*, 2015] or simulations in straight coordinates [*Liu et al.*, 2010a,b]. But *Denton et al.* [2014] recently showed that it was possible to do full scale EMIC waves simulations in dipole field geometry in a meridional plane. Here we use the same simulation code to calculate realistic two-dimensional wave fields and then examine their properties. Denton et al.'s emphasis was on the radial structure of the waves and the effects of differing composition. Here we concentrate on the latitudinal variation of the wave fields. A crucial factor affecting this variation is the geometry of the Earth's dipole magnetic field. The curvature of the field leads to refraction, and the varying magnetic field strength leads to motion of wave packets along the normalized dispersion surfaces.

A description of the linear theory relevant to the simulation follows in section 2, and a description of the simulation itself follows in section 3; the simulated wave fields are described in section 4; and a summary follows in section 5.

2 Linear Theory

Figure 1f shows linear dispersion surfaces for parallel propagation using a magnetic field of 100 nT for geostationary orbit and plasma populations with N_s, $T_{\parallel s}$, and $T_{\perp\mathrm{hot}}/T_{\parallel\mathrm{hot}}$ listed in Table 1, where N_s is the density for species s, and $T_{\parallel s}$ and $T_{\perp s}$ are the temperatures associated with thermal motion respectively parallel and perpendicular to **B**. (The other quantities in Table 1 will be discussed below in section 3.) In Figure 1f, the normalized frequency, $\omega/\Omega_{\mathrm{cp}}$, is plotted versus $k_\parallel c/\omega_{\mathrm{pi}}$, where ω is the wave angular frequency, $\Omega_{\mathrm{cp}} \equiv eB/m_p$ is the proton cyclotron frequency, m_p is the proton mass, c is the speed of light, $\omega_{\mathrm{pi}} \equiv \sqrt{N_e e^2/(\epsilon_0 m_p)}$ is the ion plasma frequency calculated using the total electron density (equal to the ion density if all particles are singly charged) and the proton mass, and ϵ_0 is the electric permittivity of free space. The curves in Figure 1f were found using the electromagnetic dispersion code WHAMP [*Ronnmark*, 1982, 1983]. Missing sections of surfaces (dotted section of the R2 surface and high $k_\parallel$ parts of the He2 and O surfaces) are highly damped.

Considering a plasma consisting of H+, He+, and O+ ions, EMIC waves can occur in three left-hand polarized (wave magnetic field rotating in a left-handed sense around **B**) wave bands [*Andre*, 1985; *Hu et al.*, 2010], the H band ("H1" with "H2" in Figure 1f), the He band ("He1" with "He2" in Figure 1f), and the O band ("O" in Figure 1f). The H band, He band, and O band waves asymptote respectively to the H+ gyrofrequency, the He+ gyrofrequency, and the O+ gyrofrequency at large values of $k_\parallel$ (see the H2, He2, and O surfaces in Figure 1f). At parallel propagation ($k_\perp = 0$), as $k_\parallel$ approaches zero, the H band frequency decreases to a cutoff ($k_\parallel = 0$) frequency above the He+ gyrofrequency, the He band frequency extends down to a cutoff frequency above the O+ gyrofrequency, and the O band uniquely extends down to zero frequency (see the H1, He1, and O surfaces in Figure 1f).

The topology of the H and He band wave surfaces can be different, however, for finite $k_\perp$. For a cold plasma and at finite wave normal angle θ_{kB} between the wave vector **k** and **B**, the wave surfaces for parallel propagation split into parts that interconnect. In that case, for surfaces similar to those in Figure 1f ("similar to" because Figure 1f is not for a cold plasma), the high-frequency part of the right hand polarized service, R3, connects to H1; the high-frequency part of the H band surface, H2, connects to the medium frequency part of the right hand polarized surface, R2, and then to the low-frequency part of the He band surface, He1; and the high-frequency part of the He band surface, He2, connects to the low-frequency part of the right hand polarized surface, R1. In this case, the O band surface would be the only one that would not connect to another surface. Then traveling down the H2 or He2 surface, there there would be crossover frequencies ("X" symbols in Figure 1f) at which the polarization would switch from left-hand to right hand and pos-

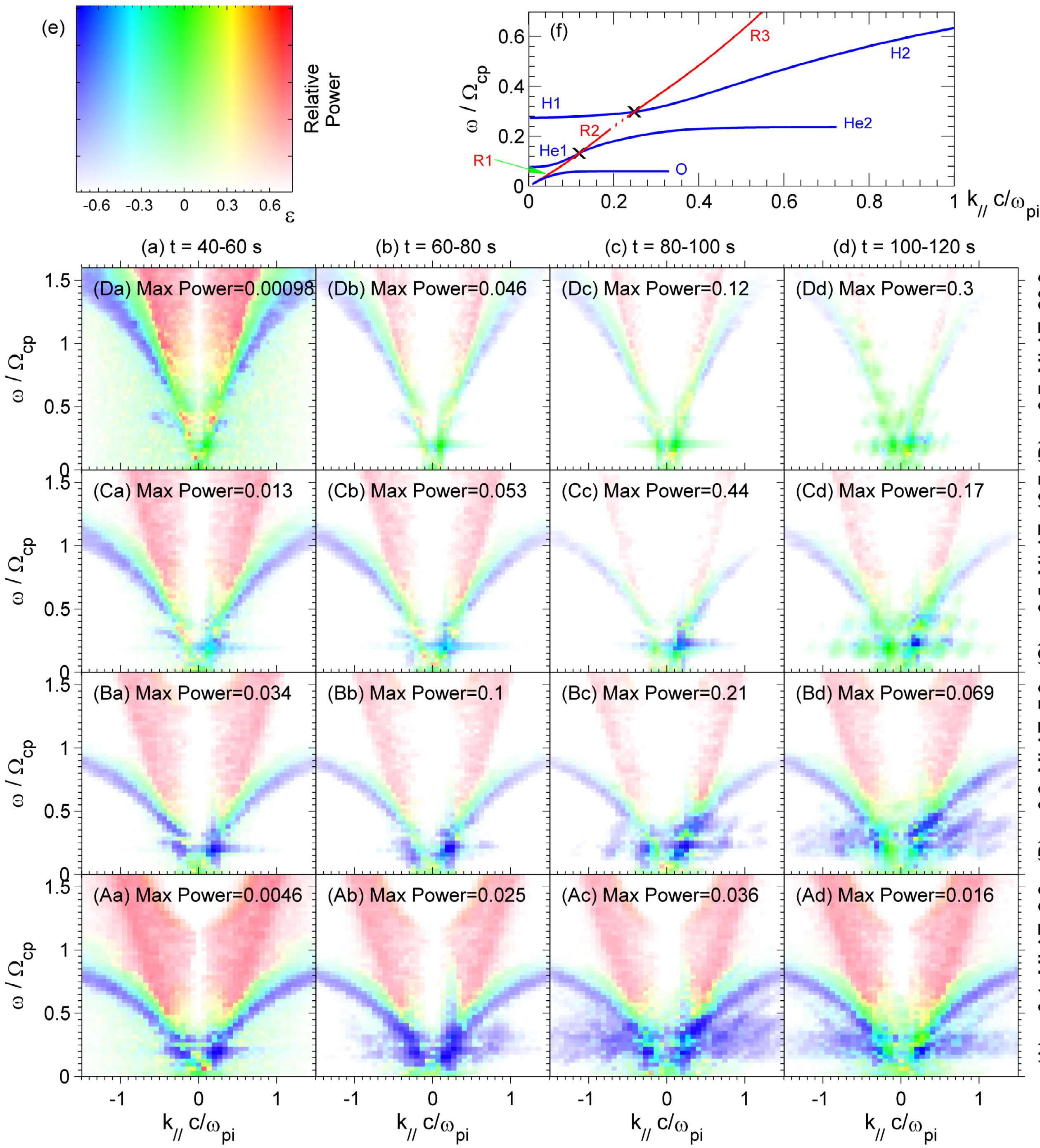

Figure 1. (f) Linear dispersion surfaces (curves) of ω/Ω_{cp} versus $k_{\|}c/\omega_{pp}$ at parallel propagation, where blue and red color is used respectively for left and right hand polarization and the other symbols are described in the text; and, in the bottom 4 by 4 set of panels, wave power dB^2/B_0^2 per unit $(k_{\|}c/\omega_{pp})(\omega/\Omega_{cp})$ versus $k_{\|}c/\omega_{pp}$ on the horizontal axis, and ω/Ω_{cp} on the vertical axis, at times (a) t = 40–60 s, (b) t = 60–80 s, (c) t = 80–100 s, and (d) t = 100–120 s, and within the boxes of Figure 3 centered at (A) q = 0.1, (B) q =0.3, (C) q = 0.5, and (D) q = 0.7. The color scale is different in each panel. The hue (particular color) indicates the ellipticity as indicated in the 2D color bar in (e), but the variation from white to saturated color represents logarithmic variation with 6 orders of magnitude up to the maximum power indicated in each panel.

Table 1. Simulation Parameters at the normalization point, $(q, r) = (0,1)$

Species s	N_s (cm^{-3})	$T_{\parallel s}$ (keV)	$\beta_{\parallel s}$	$\frac{T_{\perp s}}{T_{\parallel s}}$	$p_s{}^a$	$\frac{\text{particles}}{\text{cell}}$
Hot H+	1	10	0.403	2	6	8192
Cold H+	27.6	0.002	0.002	1	4	256
Cold He+	0.9	0.002	7×10^{-5}	1	4	256
Cold O+	0.5	0.002	4×10^{-5}	1	4	256
Cold e-	30	0	0	NA	$N_{\rm e} = N_{\rm ion}$	NA

^{a}The density of each species varies across field lines like L^{-p_s}.

sibly back again (for the H2/R2/He1 surface). Also, for both of these modes there is a bi-ion resonance at large $k_\perp$, above the He+ gyrofrequency for the H (H2/R2/He1) band or above the O+ gyrofrequency for the He (He2/R1) band [*Andre*, 1985]. (This occurs for large perpendicular component of the wave vector, and is not shown in Figure 1f.) The resulting topology is quite complex; see the descriptions by *Andre* [1985] and *Hu et al.* [2010], and especially by *Hu* [2010].

The topology of the cold plasma dispersion relations is not always applicable to a hot plasma. For the parameters used by *Denton et al.* [2014], with a hot component of protons present, the left hand polarized surfaces at parallel propagation continued to maintain their topological integrity to quite large $k_\perp$. For the parameters used in this paper (Table 1), the dispersion surfaces appear to be similar to those for a cold plasma at sufficiently large $k_\perp$. But for $k_\perp/k_\parallel$ up to about 1/8, the surfaces for parallel propagation appear to be relevant.

Figure 2 shows properties of a dispersion surface from a WHAMP run using the plasma parameters listed in Table 1, but with the hot anisotropic H+ population modified for magnetic latitude MLAT = 20.9°, as described in Table S1 of the Supplementary Information file. As we will see shortly, 20.9° was the largest MLAT value at which we calculated wave properties, and large MLAT is where we expect that the waves will be most oblique and where the details of the dispersion surfaces will be most important. (But the difference in the wave surfaces at different MLAT is not great because the plasma is dominated by the cold components that have zero anisotropy (isotropic temperature) leading to constant density along the field line [*Hu and Denton*, 2009].) The locally normalized growth rate, $\gamma/\Omega_{\rm cp,local}$, is plotted in Figure 2a, and the ellipticity is plotted in Figure 2b versus $\log_{10}(k_\perp c/\omega_{\rm pp})$ on the horizontal axis and $\log_{10}(k_\parallel c/\omega_{\rm pp})$ on the vertical axis. Here $\Omega_{\rm cp,local}$ is the local proton gyrofrequency at 20.9°, which is a factor of 1.8 larger than the equatorial proton gyrofrequency, $\Omega_{\rm cp}$.

Figure 2a shows that there is positive growth rate in the high frequency ($\omega/\Omega_{\rm cp,local} >$ 0.12) portion of the plot, which is surface He2 in Figure 1f. The branch cut shown in Figure 2a divides surface He1 of Figure 1f on the left side of the cut from surface R1 of Figure 1f. In Figure 2b, blue color represents negative ellipticity, corresponding to left hand polarized waves, whereas red color represents positive ellipticity, corresponding to right hand polarized waves; white color represents zero ellipticity, corresponding to linearly polarized waves. Thus the region to the right of the branch cut in Figure 2b is right hand polarized, agreeing with our identification as surface R1 in Figure 1f. The plateau in frequency at the bottom right corner of Figures 2a and 2b is the O-He bi-ion frequency mentioned above. If we were to extend the lower left-hand portion of Figures 2a and 2b to the right beyond the branch cut, the wave frequency eventually increases steeply with respect to $k_\perp$, becoming right hand polarized and damped. This part of the surface would be R2 in Figure 1f.

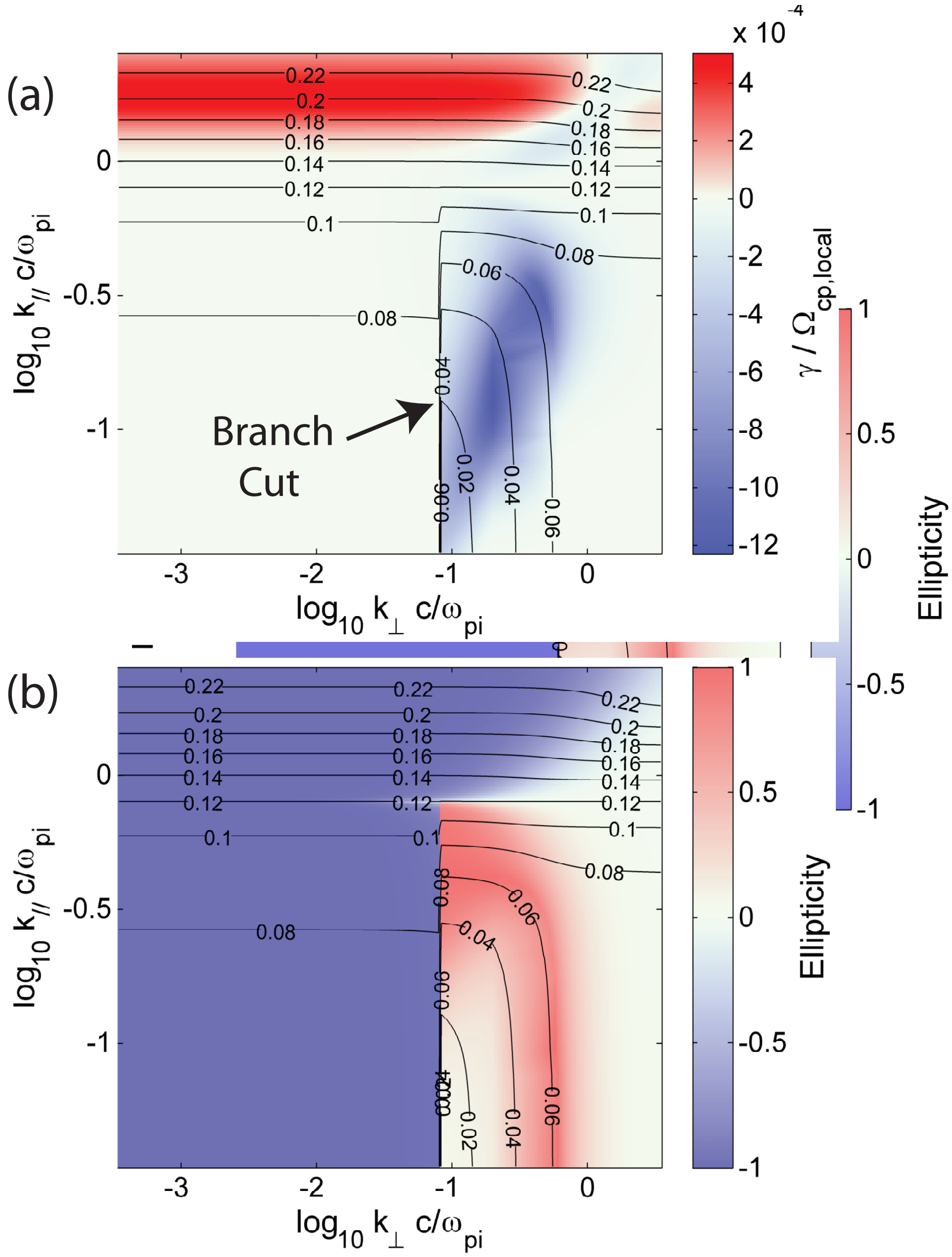

Figure 2. Dispersion surfaces from WHAMP at MLAT = 20.9°. (a) Locally normalized growth rate, $\gamma/\Omega_{\mathrm{cp,local}}$ and (b) ellipticity versus $\log_{10}(k_\perp c/\omega_{\mathrm{pp}})$ on the horizontal axis and $\log_{10}(k_\parallel c/\omega_{\mathrm{pp}})$ on the vertical axis, using the color bars at the right side of the figure. The black curves are contours of the locally normalized wave frequency, $\omega/\Omega_{\mathrm{cp,local}}$, with levels at multiples of 0.02. The discontinuity in frequency marked "Branch Cut" in panel (a) is a jump between surfaces He1 and R1 of Figure 1.

We will be running our simulation of EMIC waves over a timescale of about 100 s, corresponding to about 1000 Ω_{cp}^{-1} for an equatorial magnetic field of 100 nT. In Table S1 of the Supplementary Information file, we show instability parameters for the O, He, and H mode at four different latitudes. We estimate that the growth rate must be at least 4×10^{-3}, leading to 4 growth times in 1000 Ω_{cp}^{-1}, or an increase of a factor of $e^4 = 55$, for observable waves to grow out of the numerical noise. From the results shown in Table S1, local growth can be observed up to MLAT = 13.7° for the He mode, but only up to 7.9° for the H mode, and no local growth of O mode waves will be observable.

The maximum growth rate shown in Figure 2a, $5.05 \times 10^{-4}\Omega_{cp}$, is not large enough to cause wave significant growth in the time of our simulation. But waves can propagate from the magnetic equator to this latitude. As discussed by *Denton et al.* [2014], EMIC waves are usually most unstable in the vicinity of the magnetic equator where the temperature anisotropy of the hot protons, $A_{hot} \equiv T_{\perp hot}/T_{\| hot} - 1$, and plasma beta are largest [*Hu and Denton*, 2009; *Hu et al.*, 2010]. The group velocity of EMIC waves is approximately along the magnetic field, so EMIC wave energy propagates along the magnetic field away from the magnetic equator toward the ionosphere. As the waves propagate toward the ionosphere, the wave frequency remains constant, but the gyrofrequencies of the various ion species increase due to the increasing magnetic field. Because of this, the normalized wave frequency, ω/Ω_{cp}, decreases, so the waves move downward on the normalized wave surfaces in Figure 1f. At the same time, the waves refract outward because of the curvature of the magnetic field.

If the waves propagate onto the right hand polarized surface on the right side of the branch cut in Figure 2b, they will reflect when they reach the O-He bi-ion frequency at high MLAT. If, on the other hand, they manage to stay on the left side of the branch cut in Figure 2b, they would reflect at the cutoff frequency for the He1 surface or where the frequency on the R2 surface (joining to the He1 surface) starts to increase. There is also the possibility of tunneling to the O wave band [*Johnson and Cheng*, 1999].

In any case, if the waves refract strongly before reflecting, the polarization of the reflected waves will be linear, because all waves become more electrostatic and linear at large θ_{kB}. (See the white color in Figure 2b at large $k_\perp$.)

3 Simulation of wave fields

The following description of the hybrid code simulation is similar to that of *Denton et al.* [2014]. The hybrid code was described in detail by *Hu and Denton* [2009] and *Hu et al.* [2010]. Particles are used for the ions, while the electrons are described by an inertialess fluid. The plasma is quasi-neutral, so the electron density is equal to the ion density. The magnetic field is advanced using Faraday's law. The electric field is found from $\mathbf{E} = -\mathbf{V}_e \times \mathbf{B} + \eta\mathbf{J}$, where $\mathbf{B}$ is the magnetic field, $\mathbf{J} = \nabla \times \mathbf{B}/\mu_0$ (Ampere's law), $\mathbf{V}_e$ is the electron velocity found using $\mathbf{J} = \mathbf{J}_i - eN_e\mathbf{V}_e$, $\mathbf{J}_i$ is the ion current density, and μ_0 is the vacuum permeability. The resistivity η is nonzero only near the boundaries, where it damps the waves [*Hu and Denton*, 2009]; other than at these boundary regions, the parallel electric field is zero. Therefore one limitation of our simulation is that there is no electron Landau damping. Landau damping would cause a reduction in obliquely propagating waves, that is, waves with wave vector not parallel to $\mathbf{B}$, especially at the larger latitudes and at late times where reflected waves may be highly oblique [*Hu et al.*, 2010]. (As will be discussed in section 5, the dominant waves in this simulation are probably not greatly affected by Landau damping.)

The hybrid code uses generalized orthogonal coordinates [*Arfken*, 1970], and here we employ dipole coordinates. The inner and outer L shell boundaries are along dipole field lines. But the background magnetic field in the interior of the simulation domain is not exactly exactly dipolar. The initial magnetic field was derived from an anisotropic

MHD simulation to get a near-equilibrium initial state [*Hu et al.*, 2010]; but the initial state is still not a true equilibrium, and in this case, there are initially some small amplitude large-scale oscillations, most clearly seen in the parallel fluctuations. (The large-scale color pattern in Figure 3Ab appears to be associated with an Alfven wave.) Once the EMIC waves grow to large amplitude, however, they totally dominate the wave power.

The simulations are two dimensional representing a meridional plane. Only the northern half of this plane is simulated; symmetry conditions are used at the magnetic equator. The first coordinate q varies along the dipole magnetic field with value 0 at the magnetic equator and a value of 1 at our ionospheric boundary. The ionospheric boundary is at a magnetic latitude MLAT of 47° for the central L shell in the simulation. This range of latitude is large enough that the waves have passed through all relevant resonant surfaces before they reach the ionospheric boundary where they are damped. The q coordinate is chosen so that equal spacing in q corresponds to a distance in real space proportional to B along the central L shell in the simulation. (Since the coordinates are orthogonal, surfaces of constant q are also surfaces of the usual dipole coordinate that is orthogonal to L. There is freedom to choose a particular mapping between q and distance only at one particular L shell.) Since flux tubes have area $\propto 1/B$, the volume of each cell in the simulation is exactly constant along the central field line and roughly constant at other L values; this is a good choice for simulation of Alfvén waves, and leads to a relatively even distribution of particles, which is good for keeping the numerical noise low. The second coordinate in our simulation is the normalized dipole L value, $r = L/L_0$, where $L_0 = 6.6$ is the central L shell. We use a range of r of 0.96 to 1.04, corresponding to L varying from $L_1 = 6.34$ to $L_2 = 6.86$. The third coordinate is s, which is in the azimuthal direction eastward.

We assume a plasmasphere or plasmaplume-like plasma with $N_\mathrm{e} = 30$ cm^{-3}. In Table 1, we list the run parameters at the normalization point, which is at the middle r value ($r = 1$) at the magnetic equator ($q = 0$). The parallel plasma beta of the hot H+, $\beta_{\|\mathrm{hot}} \equiv N_\mathrm{hot} T_{\|\mathrm{hot}}/(B^2/(2\mu_0)) = 0.403$. With $T_{\perp\mathrm{hot}}/T_{\|\mathrm{hot}} = 2$, the plasma is very unstable, although not beyond the range of realistic conditions. Our ion inertial scale length, $d_\mathrm{i} \equiv c/\omega_{pi} = 41.4$ km = 0.00652 R_E. The simulation is full scale; that is, the ratio of the simulation d_i to R_E is realistic. We used 769 grid points along the dipole magnetic field (q direction) and 97 across the magnetic field (r direction). These values were chosen in order to well resolve the relevant spatial scales. There are about 25 grid points per dominant parallel wavelength at the magnetic equator, and these waves are also resolved at higher latitude. At the central L shell, there were about 4 grid points per thermal gyroradius of the hot protons. In order to achieve low simulation noise, we used 8192 particles per grid point to simulate the ring current H+ and 256 particles per grid point to simulate each of the three remaining particle populations, cold H+, cold He+, and cold O+.

In the initialization, $T_\mathrm{hot} \equiv 2T_{\perp\mathrm{hot}}/3 + T_{\|\mathrm{hot}}/3$ was set to be constant across L shells (flux surfaces), but N_s varied like L^{-p_s}, with the power law coefficients p_s equal to 4 for the cold species, and 6 for the hot protons. The L^{-4} dependence for cold species is typical in the outer magnetosphere [*Denton et al.*, 2004], whereas L^{-6} for the hot density combined with constant T_hot and $B \approx L^{-3}$ means that $\beta_\mathrm{hot} \equiv N_\mathrm{hot} T_\mathrm{hot}/(B^2/(2\mu_0))$ was roughly constant across L shells [as sometimes approximately occurs, e.g. *Lui et al.*, 1987]. The hot H+ anisotropy $A_\mathrm{hot} \equiv T_{\perp\mathrm{hot}}/T_{\|\mathrm{hot}} - 1$ was set to $2\cos((\pi/2)(L - L_0)/(L_2 - L_0))$ at the magnetic equator, which means that the plasma was unstable in the middle L shall region of the simulation domain, but was stable near the L boundaries, where $A_\mathrm{hot} = 0$. Along the field lines, the density and temperature of the cold species was constant, but the density and temperatures of the hot protons varied along the field lines in accordance with anisotropic equilibrium [*Hu and Denton*, 2009].

A major goal of deriving these simulation fields is to use them in test particle simulations of radiation belt particle dynamics. Because of this, we didn't want any wave power at grid scales, which are not accurately described in a finite difference simulation.

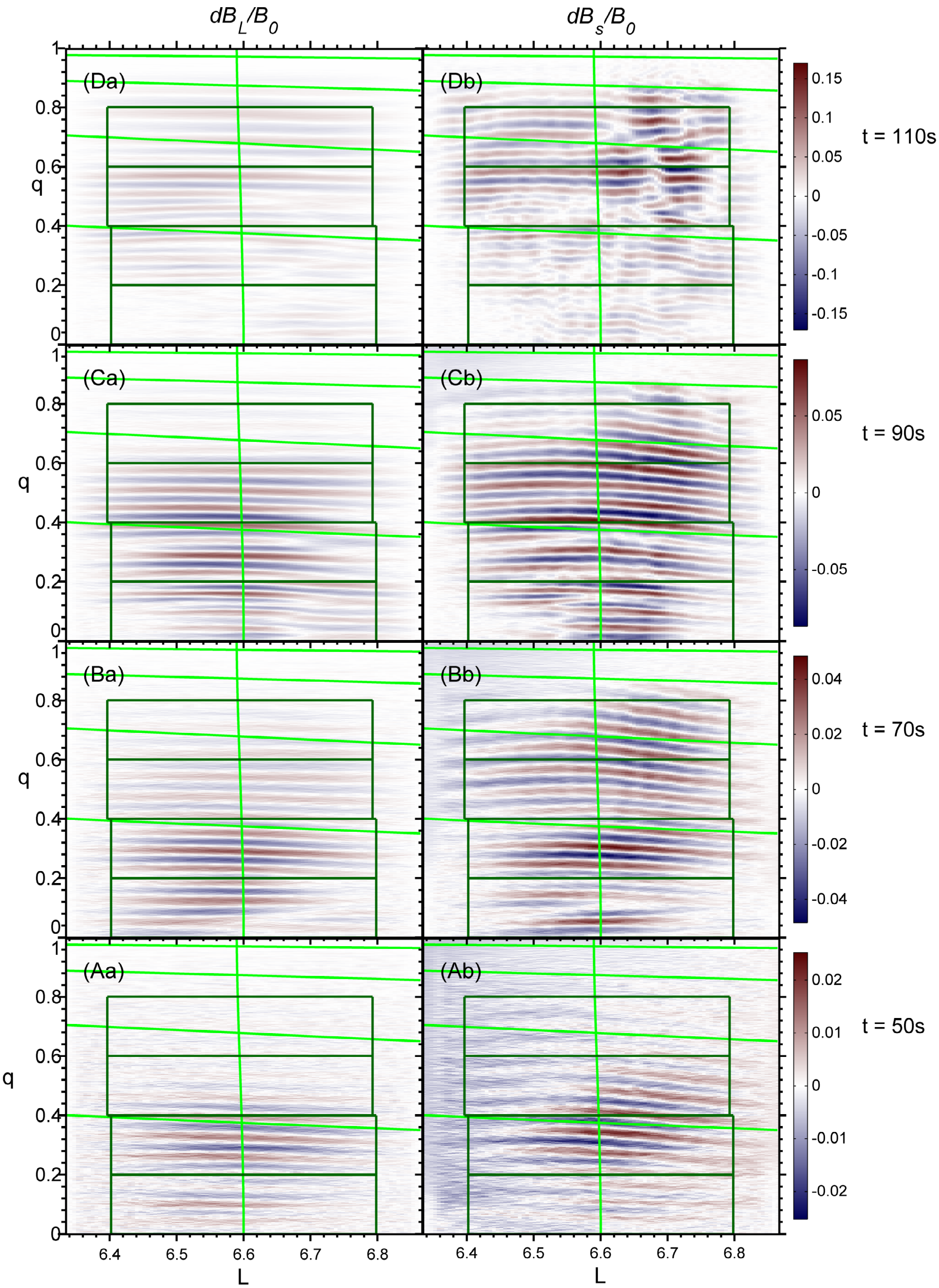

Figure 3. Left column (a) Component of wave magnetic field in the L direction perpendicular to the flux surfaces, dB_L, and right column (b) azimuthal component, dB_s, positive into the page, at the four times listed on the right side of the figure; both components are normalized to the background equatorial magnetic field, B_0. The roughly horizontal green curves are at MLAT = 10° (lowest curve), 20°, 30°, and 40° (highest curve), while the nearly vertical green curve is the central equilibrium flux surface. The black boxes enclose regions used for Fourier analysis, as described in the text.

We ran our simulation using spatial smoothing at each time step (a 0.25/0.5/0.25 averaging stencil [*Birdsall and Langdon*, 1985] applied in each direction to the electric field, the ion current density, and the ion charge density in a way that preserves energy conservation). Finally, in order to entirely eliminate grid scale structure, we filtered the electric and magnetic fields of the saved data in Fourier space, zeroing out modes with wave number greater than half the maximum (Nyquist) value in each direction. (This filtering is not energy conserving, but is only applied to the wave fields after the simulation is finished.)

4 Simulation wave fields

The wave fields grow spontaneously from the simulation noise. In Figure 3, we show the wave magnetic field, normalized to the background magnetic field at the normalization point, at four times, $t = 50$ s, 70 s, 90 s, and 110 s. The roughly horizontal green curves in each panel are at MLAT = 10° (lowest curve), 20°, 30°, and 40° (highest curve). The central nearly vertical green curve in each panel is the equilibrium flux surface connecting to the normalization point at $q = 0$; this is not exactly dipolar, which would be a vertical line in the plot. The L component in Figure 3a (first column) is perpendicular to the equilibrium flux surfaces rather than being strictly in the dipole r direction; positive s component is into the page. At each time, the equilibrium field is found by averaging the field between a time 10 s earlier and a time 10 s later. Then the instantaneous perturbed field $d\mathbf{B}$ is found at the times indicated by subtracting that equilibrium field.

The waves grow at early times (see Figure 3A, the bottom panels) in the middle region of L, where A_{hot} peaks, and close to the magnetic equator, where $\beta_{\|\mathrm{hot}}$ is largest. (The magnetic field increases at large q toward the ionospheric boundary. Also, in anisotropic equilibrium, the hot density and anisotropy decrease at large q.) The waves do not grow exactly at the magnetic equator ($q = 0$) because of the symmetry boundary condition, which causes the wave fields to be zero there. At later times (upper panels in Figure 3), the wave fields have propagated upward close to the ionospheric boundary ($q = 1$).

Close to the equator, dB_L is nearly equal to dB_s, which would be expected for parallel propagating waves with circular polarization. Near $q = 1$, however, the azimuthal component, dB_s, is larger than the L shell component, dB_L, as expected for waves that are becoming more linearly polarized. (Because of Faraday's law, and the fact that the gradients are only in the meridional plane, dB_s is larger than dB_L, which is usually the case also for observations.) Note also that the wave patterns of dB_L (Figure 3a) have wave vector that is much closer to being parallel (nearly horizontal wave fronts) than those of dB_s (Figure 3b).

The interference patterns in Figure 3Db suggest that there is considerable reflection of waves at $t = 110$ s [see *Hu et al.*, 2010], and that the reflected waves are significantly oblique, leading to interference dominantly for dB_s rather than dB_L. Note that the resistive layer (section 3) is only between $q = 0.97$ and 1, so the observed reflection, strongest between $q = 0.8$ and 0.9 (Figure 3Db), must be occurring at a natural frequency for the dominant He wave band, at the O-He bi-ion frequency or possibly the He cut-off frequency.

4.1 Frequency distribution

Figure 4 shows the wave power of transverse waves versus frequency for time intervals of 20 s centered on the times used for Figure 3. Before calculating the frequency spectrum, the data were windowed in time using a Welch data window [*Press et al.*, 1986]. The wave components dB_L and dB_s were combined into a complex transverse field with the frequency defined such that positive frequency represents right hand polarized waves, whereas negative frequency represents left hand polarized waves [*Kodera et al.*, 1977]. The waves near the magnetic equator (Figure 4A) are dominantly left hand polarized (neg-

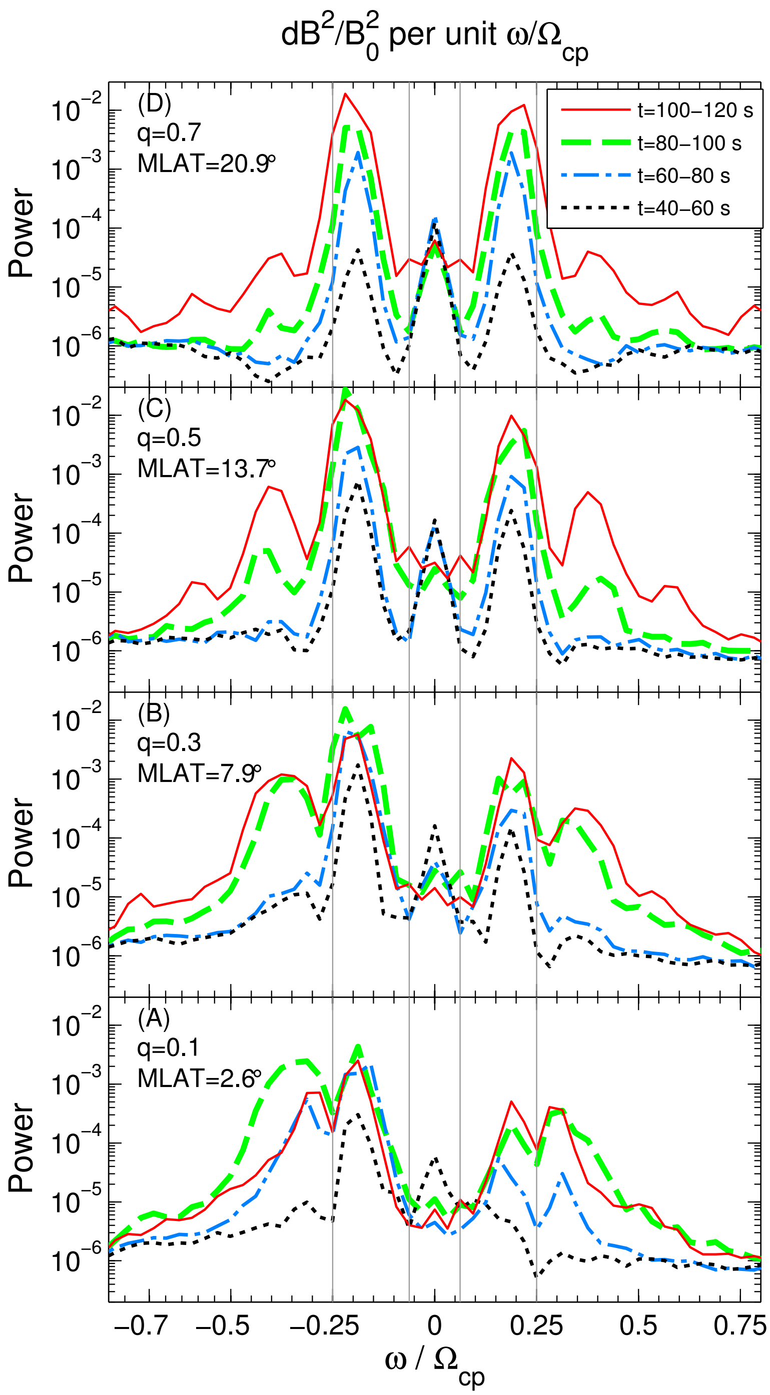

Figure 4. Wave power dB^2/B_0^2 per unit $\omega/\Omega_{\rm cp}$ versus $\omega/\Omega_{\rm cp}$ within the boxes of Figure 3 centered at (A) $q = 0.1$, (B) $q = 0.3$, (C) $q = 0.5$, and (D) $q = 0.7$. The dotted black, dash–dot blue, dashed green, and solid red curves show the wave power for the time intervals indicated in the legend of panel (D).

ative frequency), although there is some mixture of left and right hand polarization. But at the largest range of q centered on $q = 0.7$, the wave power in the negative and positive frequencies is almost equal, indicating linear polarization.

The gray vertical lines in Figure 4 are at the O+ and He+ gyrofrequencies, 1/16 and 1/4 the proton gyrofrequency, respectively. The wave power at zero frequency is an artifact of how the power spectrum is calculated, and can be ignored. There is very little if any wave power in the O+ EMIC wave band below the O+ gyrofrequency (between the two innermost vertical gray lines). That is consistent with the fact that the linear growth rate for the O+ mode is small. The first time interval for which the power spectrum is calculated is for $t = 40$–60 s, plotted as the dotted black curves. The dominant early wave growth is in the He+ EMIC waveband between $|\omega/\Omega_{\rm cp}| = 1/16$ and 1/4. At $q = 0.1$, close to the magnetic equator, the peak in wave power drops sharply at the upper frequency limit for the He+ band, $|\omega/\Omega_{\rm cp}| = 1/4$. At larger q values, the He+ mode peak in wave power overlaps $|\omega/\Omega_{\rm cp}| = 1/4$, suggesting that there are some locally generated waves at the higher latitudes. This is because the frequency of waves is constant as they propagate along the magnetic field line. So if the waves had simply propagated from near the magnetic equator, there would also be a steep drop in wave power at $|\omega/\Omega_{\rm cp}| = 1/4$ at the larger q values. Note that our normalization is to the proton gyrofrequency at the magnetic equator ($q = 0$), and the normalized frequency at higher q would be lower if the local gyrofrequency were used for the normalization. Thus it appears that the waves at $|\omega/\Omega_{\rm cp}| = 1/4$ are generated locally at larger q where the locally normalized wave frequency is lower. At later times (progressing from the blue to green to red curves), there is also wave growth in the H EMIC wave band at frequencies above $|\omega/\Omega_{\rm cp}| = 1/4$.

Note the progression of wave power along the field line away from the magnetic equator. The He band wave power in Figure 4A ($q = 0.1$) and Figure 4B ($q = 0.3$) reaches its highest values for the last three time intervals (blue, green, and red curves); but in Figure 4C ($q = 0.5$), the maximum He band wave power occurs only for the last two time intervals (green and red curves); and in Figure 4D ($q = 0.7$), the maximum He band wave power occurs only at the last time interval (red curve). Similarly, H band wave power in Figure 4A ($q = 0.1$) does not grow appreciably until the second time interval (blue curve), but it is not observed in Figure 4B ($q = 0.3$) until the third time interval (green curve). Highest up on the field line in Figure 4D ($q = 0.7$), the H band power does not become appreciable even within the last time interval (red curve).

4.2 $k_\parallel$ distribution

Figure 5 shows the wave power versus $k_\parallel c/\omega_{\rm pp}$ in a format similar to that of Figure 4. Here the sign of $k_\parallel$ is chosen so that positive sign corresponds to waves propagating away from the magnetic equator, and negative sign corresponds to waves propagating toward the magnetic equator. (Assuming the functional form $\exp(i(\omega t - k_\parallel s))$, waves propagate in the positive s direction if the Fourier transformed $k_\parallel$, has the same sign as ω.) In general, there is a preference for waves propagating in the positive direction away from the magnetic equator; each peak at negative $k_\parallel$ in Figure 5 is smaller than the corresponding peak at positive $k_\parallel$. But there are some regions where significant wave growth in the negative direction occurs.

The time evolution of the $k_\parallel$ distribution of wave power is more complicated than that of the frequency. The initial waves (black curves) are strongly dominant in the positive direction, although there is some small growth with negative $k_\parallel$, especially at $q = 0.3$ (Figure 5B). (The early wave power overlapping $k_\parallel = 0$ may be associated with large-scale oscillations.) The wave power with positive $k_\parallel$ appears to grow in time while it propagates away from the magnetic equator. For instance, the black peak at $q = 0.1$ in Figure 5A may lead to the blue peak at $q = 0.3$ in Figure 5B, then to the green peak at $q = 0.5$ in Figure 5C, and finally to the red peak at $q = 0.7$ in Figure 5D. On the other hand, we

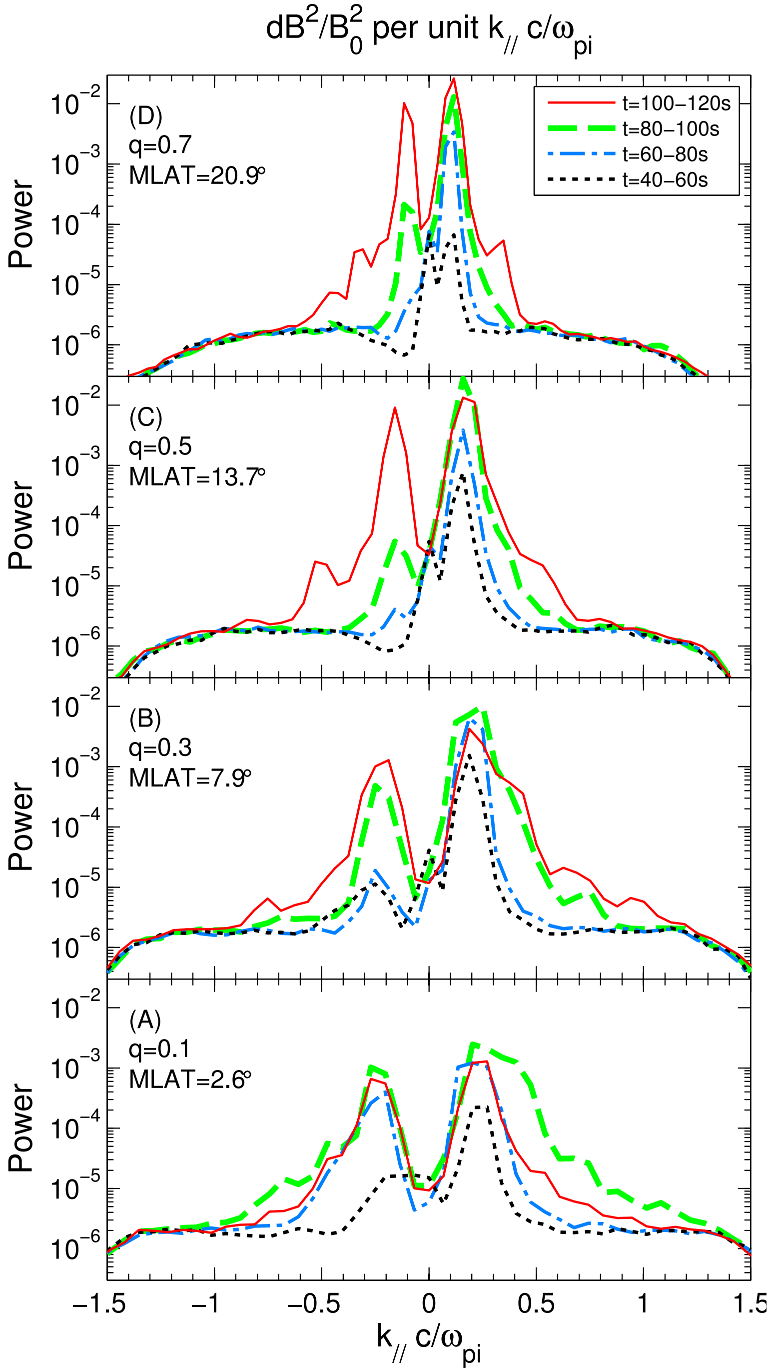

Figure 5. Wave power dB^2/B_0^2 per unit $k_\parallel c/\omega_{pp}$ versus $k_\parallel c/\omega_{pp}$ within the boxes of Figure 3 centered at (A) $q = 0.1$, (B) $q = 0.3$, (C) $q = 0.5$, and (D) $q = 0.7$. The dotted black, dash–dot blue, dashed green, and solid red curves show the wave power for the time intervals indicated in the legend of panel (D).

would not expect the waves with negative $k_\parallel$ to propagate away from the magnetic equator. Two effects may explain the development of the wave power with negative $k_\parallel$. First of all, note that the peaks at $k_\parallel c/\omega_{pp} \sim -0.25$ first grow off the equator at $q = 0.3$ (black and blue curves in Figure 5B); then the negative $k_\parallel$ wave power at about that value of $k_\parallel c/\omega_{pp}$ appears later at $q = 0.1$ (blue, green, and red curves in Figure 5A). But there is also reflection of waves, as suggested by Figure 3Db. The reflection is presumably at the O-He bi-ion frequency and is discussed more in section 4.3 below.

The peaks in $k_\parallel$ shift to smaller values at larger q (comparing Figure 5D to Figure 5A). At least for the dominant He mode, this can be explained based on the alteration of the dispersion relation due to the larger off-equatorial magnetic field. This will be demonstrated more quantitatively in section 4.4.

4.3 Distribution of wave power versus $k_\parallel$ and ω

The panels in Figure 1A–D show the distribution of wave power versus $k_\parallel c/\omega_{pp}$ on the horizontal axis and ω/Ω_{cp} on the vertical axis at the same times and positions as were used in Figure 4. Here, in order to show the different dispersion surfaces, six orders of magnitude of wave power are shown in each panel, with saturated color corresponding to the maximum wave power indicated next to the label in each panel. Blue color, green color, and red color correspond to left hand polarized, linearly polarized, and right hand polarized waves, as indicated by the two dimensional color bar (showing ellipticity and relative power) in Figure 1e.

Concentrating first on Figure 1Aa ($q = 0.1$ at $t = 40$–60 s), the blue regions represent the EMIC waves. The blue color at $\omega/\Omega_{cp} < 0.25$ is the He band, and the blue color between $\omega/\Omega_{cp} = 0.25$ and 1.0 is the H band. Note that, in agreement with Figure 1f, for which the blue curves are terminated where the damping becomes large, that the H band wave power extends out to larger $k_\parallel$ than the He band wave power. Note also that the H band extends to $\omega/\Omega_{cp} > 1$ farther from the magnetic equator (rows C and D). As mentioned in section 4.3, this is because the normalization is to Ω_{cp} at the normalization point, which is at the magnetic equator. Using the local gyrofrequency, the normalized frequency would be below unity as is normal for H band waves.

The red color at higher frequencies in Figure 1A–B is the whistler mode [see also, e.g., *Ofman et al.*, 2017]. Since the whistler mode is stable and results from noise in the simulation, it is most prominent when the maximum wave power is small (comparing Figure 1Da to Figure 1Cc).

Figure 6 is similar to Figure 1A–D except that now the variation from white to saturated color represents linear variation from zero to the maximum power indicated next to the label in each panel. This plot accentuates the dominant wave power. As was noted in reference to Figures 4 and 5, the dominant wave power is in the He band with $k_\parallel > 0$ indicating propagation away from the magnetic equator. At $t = 40$–60 s, the maximum wave power is at $q = 0.1$; at $t = 60$–80 s, the maximum wave power is at $q = 0.3$; at $t = 80$–100 s, the maximum wave power is at $q = 0.5$; and at $t = 100$–120 s, the maximum wave power is at $q = 0.7$. At $t = 60$–80 s, some wave power in the H band starts to appear at $q = 0.1$ (Figure 6Ab). Observable H band wave power propagates to $q = 0.3$ by $t = 100$–120 s (Figure 6Bd). Wave power with negative $k_\parallel$ also begins to appear at $t = 60$–80 s (Figure 6Ab). As explained in section 4.2, this wave power might have propagated toward the magnetic equator from $q \sim 0.3$. At the final time, $t = 100$–120 s (column d), wave power with negative $k_\parallel$ appears also at other positions along the magnetic field line. The later occurrence probably results mostly from reflection, though there could be some local growth with smaller linear growth rate at high latitude.

Also shown in each panel of Figure 6 are the left hand polarized surfaces (black curves) for H band (upper black curves), He band (middle black curves), and O band

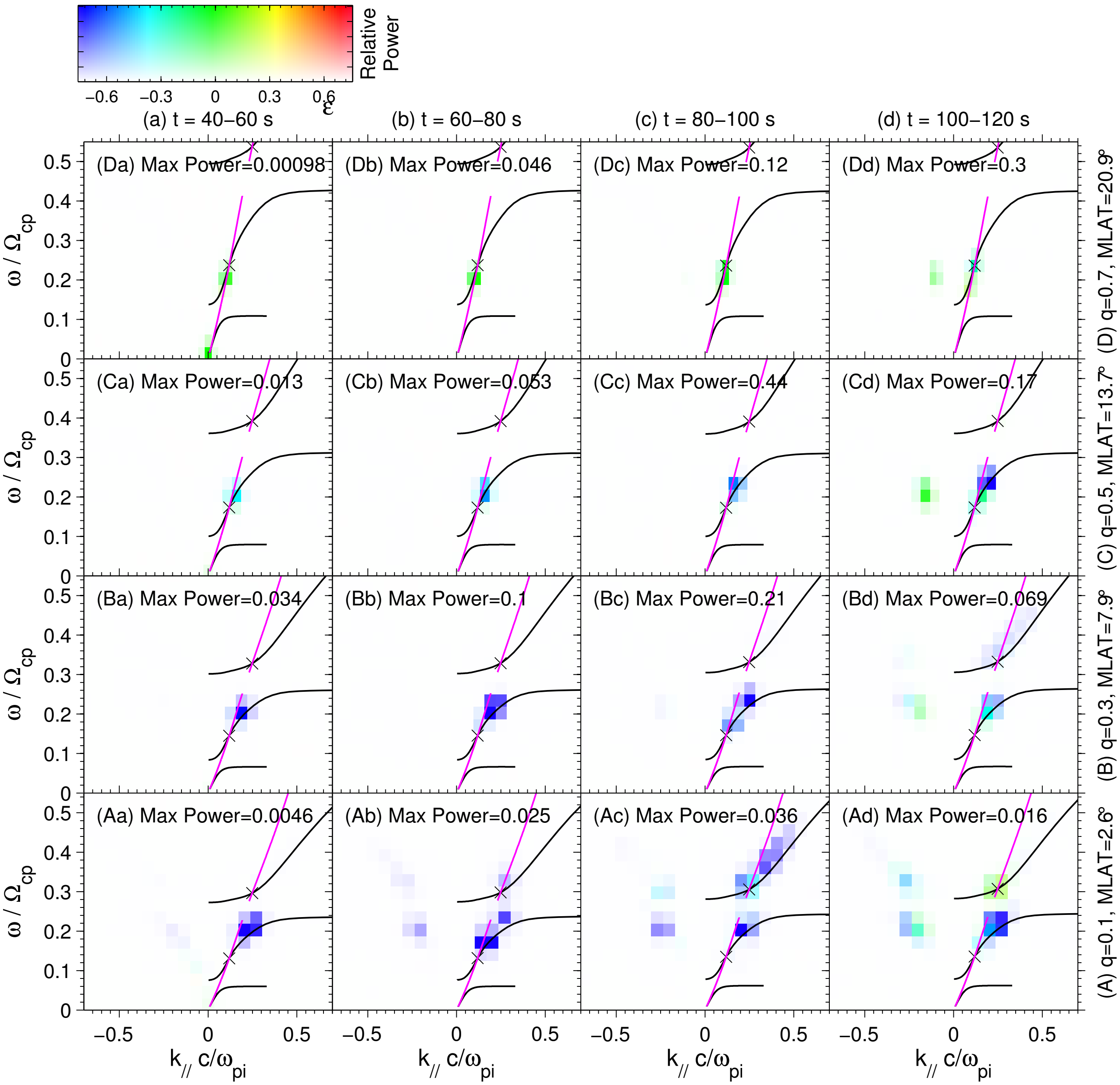

Figure 6. Wave power dB^2/B_0^2 versus $k_{\|}c/\omega_{\mathrm{pp}}$ and $\omega/\Omega_{\mathrm{cp}}$ like in Figure 6, except that here the variation from white to saturated color represents linear variation from zero to the maximum power indicated in each panel. The black curves are the linear dispersion surfaces for left-hand polarized waves and the magenta curves are the linear dispersion surfaces for right-hand polarized waves, both at nearly parallel propagation. The upper, middle, and lower curves are for the H band, He and, and O band waves. The black crosses mark the positions where the right hand polarized wave surfaces cross the left hand polarized surfaces.

(lower black curves) and right hand polarized services (magenta curves) for parallel propagating waves propagating away from the magnetic equator (positive $k_\parallel$), as were plotted in Figure 1f. Since the dispersion surfaces yield ω normalized to the local magnetic field, but the frequency in all the panels of Figure 6 (plotted on the vertical axis) is normalized to the equatorial magnetic field, we shift the equatorial dispersion relations up in frequency in the figure by the ratio of the local to equatorial magnetic field. We also show the position on the dispersion relations where the right hand polarized waves cross the left hand polarized waves as black crosses.

All of the observed waves lie close to the linear dispersion relations. As was noted earlier, the He band waves are the strongest. As the forward propagating He band waves propagate up to $q = 0.7$, the frequency of the waves is constant, and so is ω/Ω_{cp} because Ω_{cp} is the cyclotron frequency at the fixed equatorial normalization point. But if ω were normalized to the local gyrofrequency, its normalized frequency would decrease at larger MLAT. Alternately, the dispersion surfaces are rising relative to the fixed frequency of the waves. Then as the waves move down on the locally normalized dispersion surface, they also move to smaller $k_\parallel c/\omega_{pp}$. (The normalization factor for the wave vector, c/ω_{pp}, is not strongly dependent on latitude because the equilibrium cold density is constant along field lines.) This reduction in $k_\parallel c/\omega_{pp}$ is greatest at the larger latitudes where the local to equatorial magnetic field ratio is the largest. The local to equatorial magnetic field ratio is about 1., 1.1, 1.3, and 1.8 in Figure 6A, 6B, 6C, and 6C, respectively (Table S1).

The He band waves become linearly polarized when the frequency approaches the crossover frequency (black crosses), as shown in Figure 6Cd and Dd. It is possible then that the He mode wave power is transitioning through the crossover frequency from surface He2 in Figure 1f to the right hand polarized surface R1. But the polarization could also become linear because the waves are becoming highly oblique.

The He band waves started to grow high up on their linear dispersion curve, and were thus able to continue to move down the locally normalized dispersion curve, even to $q = 0.7$. Because the dispersion curve is roughly linear in that regime, it explains the previously observed variation of $k_\parallel$, expected to be roughly proportional to $1/B$. The H band wave power, on the other hand, starts growing close to the crossover frequency and not far above the He-H bi-ion frequency or cutoff frequency (low $k_\parallel$ limit) of the left-hand polarized H mode (upper curve in Figure 6A). As explained by *Denton et al.* [2014], the normalized frequency of linearly unstable waves is limited by the anisotropy such that $\omega/\Omega_{\mathrm{cp,local}} < A/(A+1)$ (their equation 7), where $\Omega_{\mathrm{cp,local}}$ is the local proton gyrofrequency. For an anisotropy of 1, the normalized frequency must be less than 0.5. The result is that the He band waves can be driven on the high-frequency part of their dispersion curve, but the H band waves must be driven on the low-frequency part of their dispersion curve. Therefore, there is not much room for the H band waves to travel down the locally normalized dispersion surface before reflecting; H band waves are strongest at $q = 0.1$ and $q = 0.3$ (Figure 6A and 6B). Within this range of MLAT, B does not vary greatly (only by 1.1 to $q = 0.3$), so not much variation is seen in $k_\parallel$ for the H band waves.

4.4 Latitudinal dependence of dominant wave

Now we plot in Figure 7 the properties of the dominant waves propagating away from the magnetic equator ($k_\parallel > 0$). At each time and latitude (q), we calculate the total wave power and the power weighted average $k_\parallel$ and ϵ for the He and H wave bands. The results are shown in Figure 7. The strongest wave power is slightly less than $2 \times 10^{-3} B_0^2$ in the He band at $q = 0.5$ (green curve in Figure 7Aa). This implies a wave amplitude of roughly $\sqrt{2 \times 10^{-3}} = 0.045 B_0$ normalized to the equatorial magnetic field, or $0.04/1.3 = 0.03$ normalized to the local magnetic field at $q = 0.5$. This is a large but not unrealistic value.

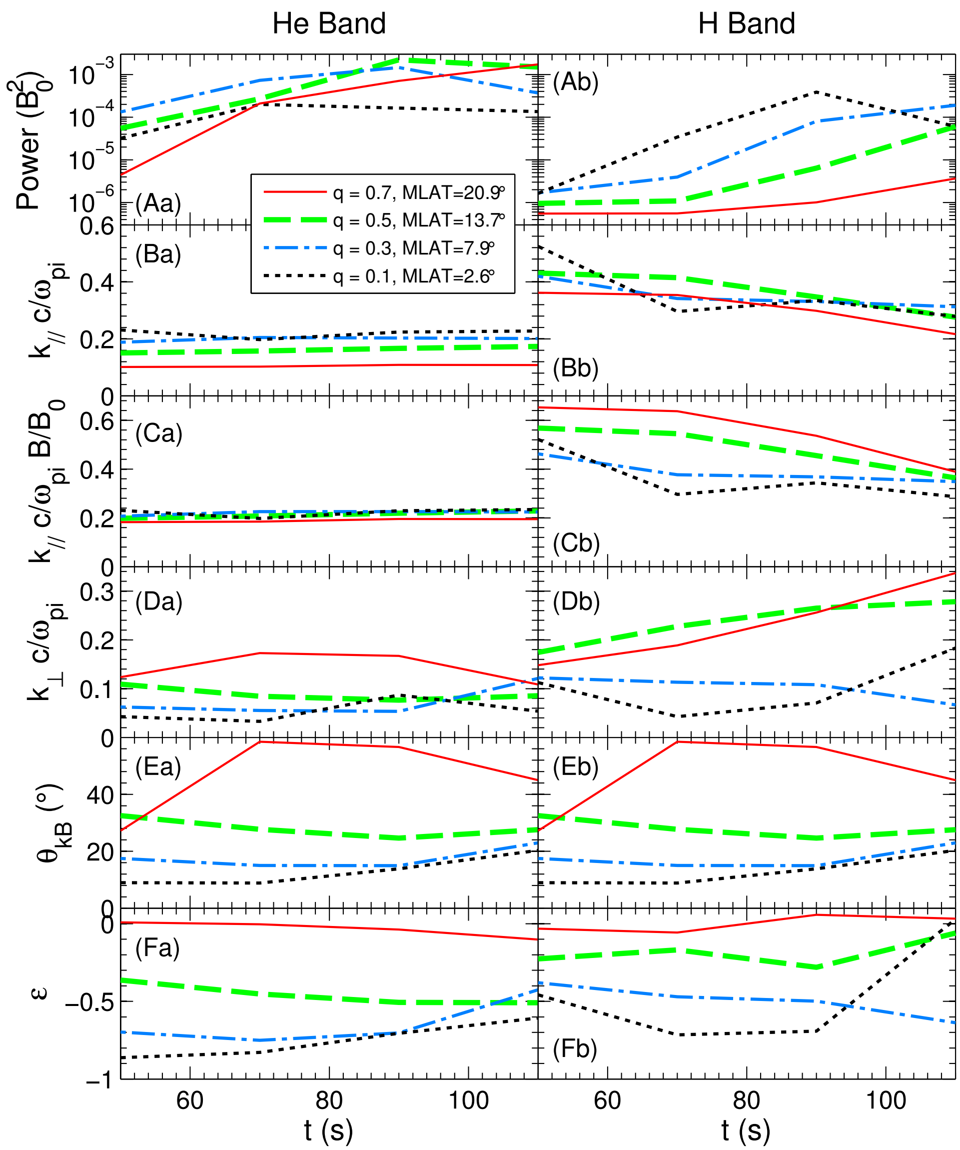

Figure 7. Properties of the dominant wave propagating away from the magnetic equator. (A) The total wave power, (B) power weighted $k_{\parallel}c/\omega_{pp}$, (C) power weighted $k_{\parallel}c/\omega_{pp}B/B_0$, (D) power weighted $k_{\perp}c/\omega_{pp}$, (E) wave normal angle θ_{kB} based on the power weighted **k** from B and D, and (F) power weighted ϵ for (a) the He band and (b) H band, versus time t. The normalization uses quantities at the magnetic equator on the central field line.

Consider first the wave power in the He band (Figure 7a). Initially, the wave power is strongest off the magnetic equator at $q = 0.3$ (blue curve in Figure 7Aa); but later, at $t = 90$ s, the strongest wave power is at $q = 0.5$ (green curve); and at the last time plotted, $t = 110$ s, the strongest wave power is at $q = 0.7$ (red curve). This implies propagation of the wave power away from the magnetic equator, as we have already discussed. The He wave power at $q = 0.7$ appears still to be growing (red curve in Figure 7a), so it might rise at later times to slightly higher values than the highest values at $q = 0.5$ (green curve). The power weighted average of $k_{\|}$ decreases at larger q (comparing the different curves in Figure 7Ba), consistent with Figures 5 and 6. But when we multiply $k_{\|}$ by B/B_0 (Figure 7Ca), the resulting product is almost invariant. This demonstrates the $k_{\|} \propto 1/B$ scaling that we discussed in section 4.3. The power weighted average ellipticity (Figure 7Fa) is more negative (more left-handed) close to the magnetic equator at $q = 0.1$, and is close to zero, indicating linear polarization, at $q = 0.7$. The ellipticity at $q = 0.1$ is most negative at the earliest time, and farther away from the magnetic equator the ellipticity is most negative when the strongest wave power propagates up to that position from close to the magnetic equator. For instance, the ellipticity is most negative at $q = 0.7$ at $t = 110$ s when the wave power reaches a maximum at that position.

Now consider the wave power in the H band (Figure 7b). In this case, the wave power never becomes large at $q = 0.7$ (red curve in Figure 7Ab), and the wave power at $q = 0.5$ (green curve in Figure 7Ab) only becomes larger than that at $q = 0.1$ (black curve in Figure 7Ab) at the end of the simulation when the wave power at $q = 1$ drops significantly. As we saw from Figure 6, the wave power in the H band generated near the magnetic equator is not able to propagate to $q = 0.7$ because at that latitude the normalized wave frequency of the equatorially generated waves has decreased below the cutoff frequency. Therefore the H band wave power observed at $q = 0.7$ must be generated locally. While some of the higher frequency portion of the H band wave power generated equatorially may be able to propagate to $q = 0.5$ (if ω/Ω_{cp} is at least as great as 0.36; see Figure 6C), the strongest wave power generated equatorially in the H band has lower frequency (see Figure 6Ac) and will not be able to propagate to $q = 0.5$. For this reason, the waves in the H band observed at $q = 0.5$ are either locally generated waves with higher frequency or waves that have propagated away from the magnetic equator, but limited to the higher frequencies. In either case, the higher frequency waves are associated with higher $k_{\|}$. For this reason, the power averaged $k_{\|}$ is not $\propto 1/B$ (Figure 7Cb) like it was for the He band because the dominant waves observed close to the magnetic equator are not the same waves that are observed at $q \geq 0.5$. Rather the wave power averaged $k_{\|}$ is almost constant with respect to q (Figure 7Bb). Like we saw for the He band, the power weighted average ϵ becomes closer to zero at larger q. The values of ϵ are a little closer to zero for the H band compared to the He B band, possibly because the H band waves are generated lower in relative frequency on their wave band or because they are not as well developed (smaller amplitude).

4.5 $k_{\perp}$ dependence

Figure 8 shows the distribution of wave power with respect to $k_{\perp}$ with respect to time (different curves) and position along the field line (different panels). Note that the precipitous drop in wave power at large $k_{\perp}$ is due to the low pass filtering to eliminate grid scale waves. As was the case for $k_{\|}$, positive $k_{\perp}$ corresponds to propagation in the positive L direction. At the earliest time close to the magnetic equator (black curve in Figure 8A), the peak in the distribution is close to $k_{\perp} = 0$ and the peak is relatively narrow. The central value of the peak and the width of the distribution both increase with increasing time and q. On the other hand, the peak values of $k_{\|}$ decrease at large q, at least for the dominant He band waves, due to the motion of the locally normalized wave frequency down the dispersion relation, as discussed in section 4.3. These opposite trends coordinate with the turning of the wave fronts to become more oblique at large q.

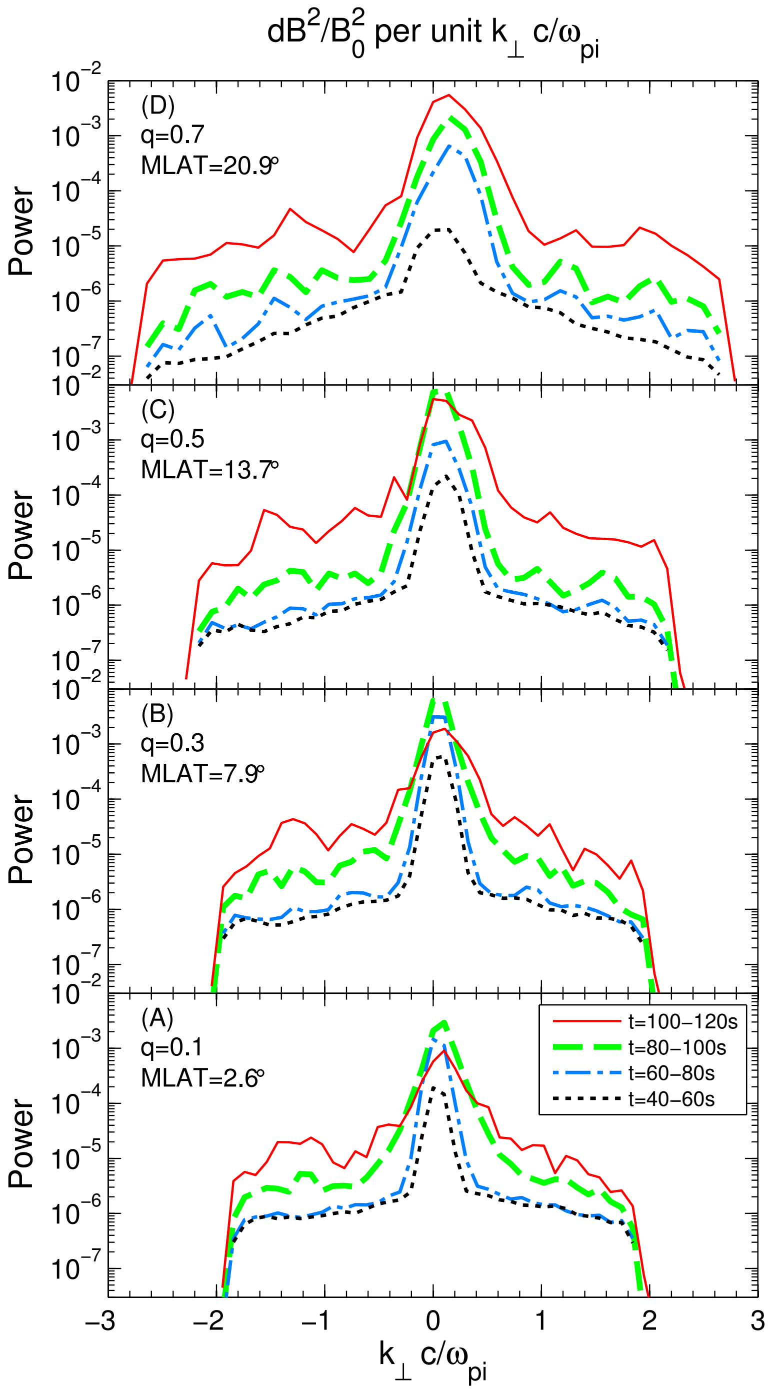

533 **Figure 8.** Wave power dB^2/B_0^2 per unit $k_\perp c/\omega_{\rm pp}$ versus $k_\perp c/\omega_{\rm pp}$ within the boxes of Figure 3 centered at (A) $q = 0.1$, (B) q =0.3, (C) $q = 0.5$, and (D) $q = 0.7$. The dotted black,dash–dot blue, dashed green, and solid red curves show the wave power at the times indicated in the legend of panel (A).

Figure 7, discussed in section 4.4, shows the power weighted average $k_\perp c/\omega_{pp}$ (Figure 7D) and wave normal angle $\theta_{kB} = \tan^{-1}(k_\perp/k_\parallel)$ (Figure 7E) using the wave power weighted average values of **k** for He band (Figure 7a) and H band (Figure 7b) waves propagating away from the magnetic equator ($k_\parallel > 0$). Because the waves refract outward as they propagate away from the magnetic equator [*Denton et al.*, 2014], the values of $k_\perp c/\omega_{pp}$ and θ_{kB} are larger farther away from the magnetic equator (comparing, e.g., the red curves in Figure 7D and E to the black curves).

Figure 9 shows the wave power distribution for the He band waves versus $k_\parallel c/\omega_{\rm pp}$ and $k_\perp c/\omega_{\rm pp}$ within the boxes of Figure 3 at four different locations along the field line in the four time intervals studied in this paper. Similarly, Figure 10 shows the same information, but for the H band waves. These plots show many features already mentioned, the transition to linear polarization, the decrease in $k_\parallel$, and the broadening and shift of $k_\perp$ to more positive values at large q. Figures 9 and 10 also show that $k_\perp$ shifts to more positive values (outward propagation) for negative as well as positive $k_\parallel$.

4.6 Data files

In the Supplementary Information file, we describe data files for this paper. These include time-dependent values of the q, r, and s components of the magnetic and electric field (data set ds01); the instantaneous parallel, L, and s components of the magnetic and electric field at the four times shown in Figure 3 (ds02); and the Fourier transformed magnetic and electric field within the boxes of Figure 3 using the four time intervals studied in this paper (ds03). All of these files are available in a Zenodo data repository. In addition, there are Matlab programs that read the data and generate a plot.

5 Summary

We have examined in detail the latitudinal evolution of electromagnetic ion cyclotron (EMIC) waves in an approximately dipole magnetic field for one particular case. The cold density is relatively high representing a plasmasphere or plume-like plasma at geostationary orbit, and the temperature anisotropy of the hot protons, $A = T_{\perp,\rm hot}/T_{\parallel,\rm hot}$ is limited to unity. The parameters vary in space such that the most unstable conditions are near the magnetic equator on the central field line.

The two main effects of the dipole geometry are curvature, which causes radially outward turning of the wave vector [*Denton et al.*, 2014], and the increase in the equilibrium magnetic field at high latitude, which causes waves that propagate away from the magnetic equator to move downward on normalized dispersion surfaces.

Waves grow out of the numerical noise near, but not exactly at, the magnetic equator. If the symmetry boundary condition at the magnetic equator were relaxed, waves might grow there [*Hu and Denton*, 2009]. As the waves propagate along magnetic field lines away from the magnetic equator, they grow and their wave vector turns radially outward, leading to linear polarization at the higher latitudes. The strongest waves propagate away from the magnetic equator, but some wave power propagating toward the magnetic equator is observed due to local generation (especially close to the magnetic equator) and reflection at high latitudes.

Since we don't have parallel electric field in the simulation, there is no Landau damping and the growth of oblique waves is likely overestimated. Consider He mode waves that propagate up to MLAT = 20.9°. We expect that the strongest He mode waves will be generated with the largest growth rate at the magnetic equator; these waves have $\omega/\Omega_{\rm cp} = 0.184$ (Supplementary Information Table S1). When He waves with $\omega/\Omega_{\rm cp} = 0.184$ arrive at MLAT = 20.9°, the locally normalized gyrofrequency, $\omega/\Omega_{\rm cp,local}$, will be a factor of 1.8 smaller, 0.104 (Table S1). Figure 2b shows that this is just below the crossover fre-

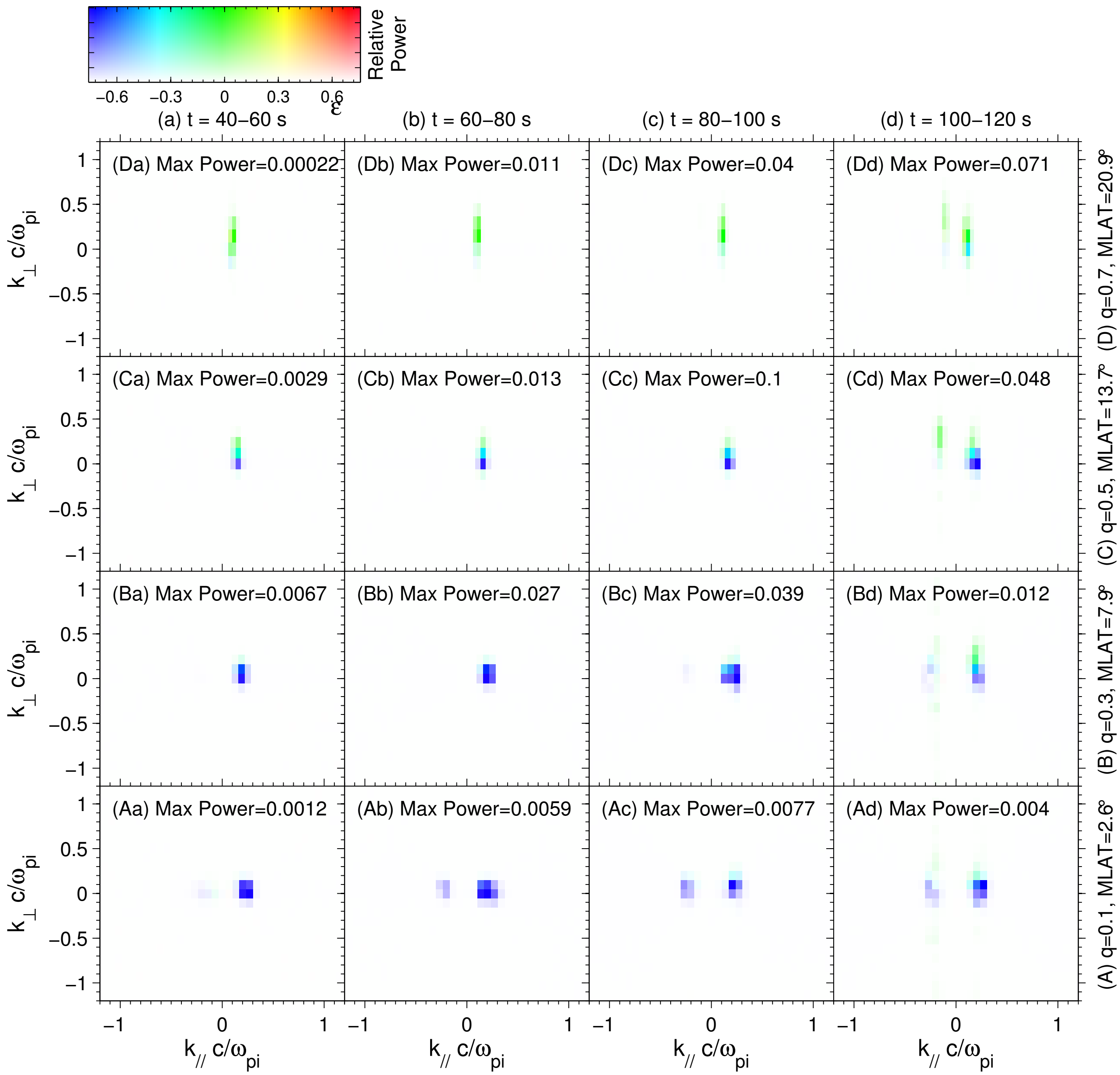

Figure 9. Distribution of wave power $(dB/B_0)^2$ versus $k_\parallel c/\omega_{\rm pp}$ on the horizontal axis and $k_\perp c/\omega_{\rm pp}$ on the vertical axis per unit $k_\parallel k_\perp (c/\omega_{\rm pp})^2$ for the He wave band within the boxes of Figure 3 centered at (A) $q = 0.1$, (B) $q = 0.3$, (C) $q = 0.5$, and (D) $q = 0.7$, for (a) $t = 40$–60 s, (b) $t = 60$–80 s, (c) $t = 80$–100 s, and (d) $t = 100$–120 s. In each panel, the wave power is plotted with a linear scale, where white represents zero wave power, and saturated color is the maximum power listed next to each panel label. The hue, or particular color, represents the ellipticity, as shown in the color scale above Figure 9Da

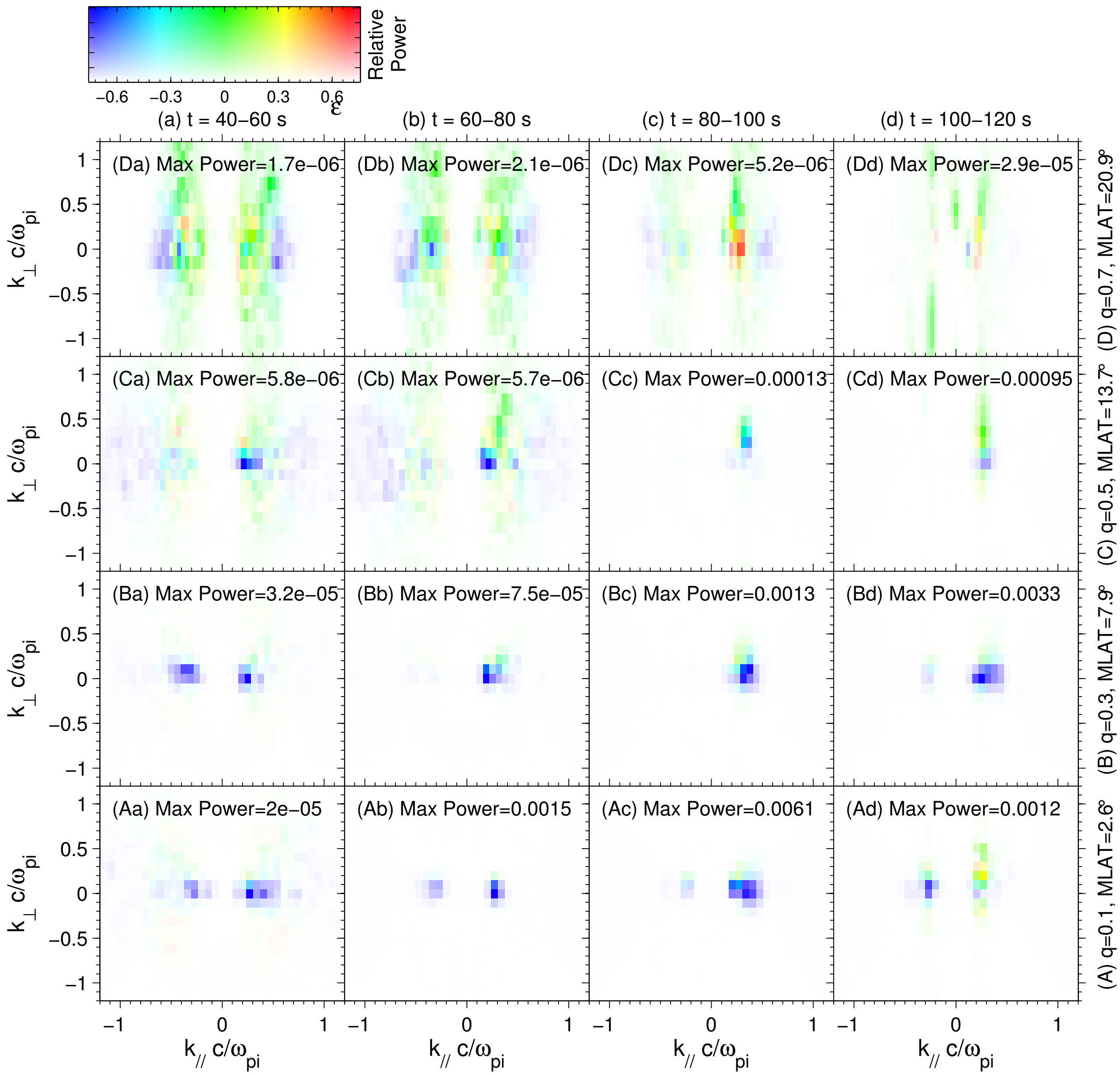

560 **Figure 10.** Similar to Figure 9, except showing the wave power distribution of the H band waves.

quency in the bottom right portion of the plot. We estimate that a damping rate will have to be as large (negatively) as -1×10^{-3} to cause significant damping in a time interval of 300 $\Omega_{\mathrm{cp}}^{-1}$ so as to make a noticeable effect in our simulation (damped by factor 1.3). On the lower right-hand surface of Figure 2a, we find that the damping rate is less than this value up to θ_{kB} of at least 81°. But the dominant waves in the simulation have θ_{kB} less than 81° (Figure 7E).

Similar results are found at smaller MLAT, for which the equatorial waves are higher up in locally normalized wave frequency. The result of this analysis is that Landau damping, neglected in our simulation, is not likely to lead to significant damping of the dominant waves that we simulate. There may be some wave damping, especially at the final time of the simulation where we see reflected waves (Figure 3D). If the simulation were run to larger times, as was done by *Hu et al.* [2010], then all the waves in the simulation would have been reflected and large θ_{kB} would result from the large spatial gradients in wave power. In that case, the effect of neglecting Landau damping might be significantly greater.

By examining the wave power in limited regions, we were able to calculate the wave vector of the waves and show how the waves move down their dispersion surface. The H band waves experienced a frequency filtering effect. Only higher frequency waves could propagate to high latitudes because the lower frequency waves were reflected when the locally normalized wave frequency decreased to the He-H bi-ion frequency or H band cutoff frequency. This effect also occurs for the He band waves, but at higher latitude than where we calculated the wave properties. Within the range of MLAT that we considered, 0° to 21°, the wave power averaged $k_\parallel$ was roughly proportional to the inverse of the local magnetic field for the He band waves, consistent with their motion along the dispersion relation. But the wave power averaged $k_\parallel$ of the H band waves was almost constant because of the frequency filtering (see section 4.4). At the same time that $k_\parallel$ decreased for the He band waves, the central value of $k_\perp$ increased and the peak broadened for both wave bands.

Our goal was to simulate waves in a local region of L shell. *Hu and Denton* [2009] showed that if a large region of L shell is unstable, the waves tend to break up into separately coherent sections.

The wave fields that we have simulated should be useful for quasi-linear and test particle simulations of radiation belt particle dynamics. In this simulation, the dominant H band waves have slightly larger $k_\parallel$ than the dominant He band waves, and some H band wave power extends to significantly higher frequency with correspondingly higher $k_\parallel$ (Figure 6Ac). This is in disagreement with equation (7) of *Denton et al.* [2015], who assume that waves in both He and H bands are in resonance with hot protons having parallel velocity equal to the hot proton parallel thermal velocity. Apparently the H band waves are driven by lower velocity protons than are the He band waves. (Note that in the simulation of *Denton et al.* [2014] used by *Denton et al.* [2015], the H band waves did not appear in the same spatial region as the He band waves; and *Denton et al.* [2015] examined only the dominant waves.) The result is that in this case the minimum resonant energy of radiation belt electrons will be lower for interaction with the H band waves, especially with the higher frequency H band waves.

Acknowledgments

Work at Dartmouth College was supported by NASA grant NNX13AD65G. The data from the simulation is available online as discussed in section 4.6.

References

Andre, M. (1985), Dispersion surfaces, *Journal of Plasma Physics*, *33*(FEB), 1–19.

Arfken, G. (1970), *Mathematical Methods for Physicists*, 2nd ed., Academic Press, New York.

Birdsall, C. K., and A. B. Langdon (1985), *Plasma physics via computer simulation*, McGraw-Hill, New York.

Denton, R. E., J. D. Menietti, J. Goldstein, S. L. Young, and R. R. Anderson (2004), Electron density in the magnetosphere, *J. Geophys. Res.*, *109*(A9), A09215, doi: 10.1029/2003JA010245.

Denton, R. E., V. K. Jordanova, and B. J. Fraser (2014), Effect of spatial density variation and O+ concentration on the growth and evolution of electromagnetic ion cyclotron waves, *J. Geophys. Res.*, *119*(10), 8372–8395, doi:10.1002/2014ja020384.

Denton, R. E., V. K. Jordanova, and J. Bortnik (2015), Resonance of relativistic electrons with electromagnetic ion cyclotron waves, *Geophys. Res. Lett.*, *42*(20), 8263–8270, doi: 10.1002/2015gl064379.

Fraser, B. J., T. M. Loto'aniu, and H. J. Singer (2006), Electromagnetic ion cyclotron waves in the magnetosphere, in *Magnetospheric Ulf Waves: Synthesis and New Directions*, *Geophysical Monograph Series*, vol. 169, edited by K. Takahashi, P. J. Chi, R. E. Denton, and R. L. Lysak, pp. 195–212, times Cited: 27 Chapman Conference on Magnetospheric ULF Waves Mar 21-25, 2005 San Diego, CA Nasa; nsf.

Hendry, A. T., C. J. Rodger, and M. A. Clilverd (2017), Evidence of sub-mev emic-driven electron precipitation, *Geophys. Res. Lett.*, *44*(3), 1210–1218, doi: 10.1002/2016gl071807.

Hu, Y. (2010), Hybrid code simulation of electromagnetic ion cyclotron waves in curvilinear coordinates, (Ph.D. dissertation), Hanover, NH: Dartmouth College, Ph.D. thesis.

Hu, Y., and R. E. Denton (2009), Two-dimensional hybrid code simulation of electromagnetic ion cyclotron waves in a dipole magnetic field, *J. Geophys. Res.*, *114*, doi: 10.1029/2009ja014570.

Hu, Y., R. E. Denton, and J. R. Johnson (2010), Two-dimensional hybrid code simulation of electromagnetic ion cyclotron waves of multi-ion plasmas in a dipole magnetic field, *J. Geophys. Res.*, *115*, a09218, doi:10.1029/2009ja015158.

Johnson, J. R., and C. Z. Cheng (1999), Can ion cyclotron waves propagate to the ground?, *Geophys. Res. Lett.*, *26*(6), 671–674, doi:10.1029/1999gl900074.

Kodera, K., R. Gendrin, and C. Devilleday (1977), Complex representation of a polarized signal and its application to analysis of ULF waves, *J. Geophys. Res.*, *82*(7), 1245–1255, doi:10.1029/JA082i007p01245.

Kubota, Y., Y. Omura, and D. Summers (2015), Relativistic electron precipitation induced by EMIC-triggered emissions in a dipole magnetosphere, *J. Geophys. Res.*, *120*(6), 4384–4399, doi:10.1002/2015ja021017.

Liu, K., D. S. Lemons, D. Winske, and S. P. Gary (2010a), Relativistic electron scattering by electromagnetic ion cyclotron fluctuations: Test particle simulations, *J. Geophys. Res.*, *115*, a04204, doi:10.1029/2009ja014807.

Liu, K., S. P. Gary, and D. Winske (2010b), Spectral properties of the Alfven cyclotron instability: Applications to relativistic electron scattering, *J. Geophys. Res.*, *115*, a08212, doi:10.1029/2009ja015201.

Lui, A. T. Y., R. W. McEntire, and S. M. Krimigis (1987), Studies of storm-time ring current from the AMPTE-CCE MEPA measurements, *Physica Scripta*, *36*(2), 378–381, doi:10.1088/0031-8949/36/2/031.

Meredith, N. P., R. M. Thorne, R. B. Horne, D. Summers, B. J. Fraser, and R. R. Anderson (2003), Statistical analysis of relativistic electron energies for cyclotron resonance with EMIC waves observed on CRRES, *J. Geophys. Res.*, *108*(A6), 1250, doi: 10.1029/2002ja009700.

Millan, R. M., and R. M. Thorne (2007), Review of radiation belt relativistic electron losses, *J. Atmos. Sol.-Terr. Phys.*, *69*(3), 362–377, doi:10.1016/j.jastp.2006.06.019.

Ofman, L., R. E. Denton, J. Bortnik, X. An, A. Glocer, and C. Komar (2017), Growth and nonlinear saturation of electromagnetic ion cyclotron waves in multi-ion species magnetospheric plasma, *J. Geophys. Res.*, *122*(6), 6469–6484, doi:10.1002/2017ja024172.

Omura, Y., and Q. Zhao (2012), Nonlinear pitch angle scattering of relativistic electrons by EMIC waves in the inner magnetosphere, *J. Geophys. Res.*, *117*, a08227, doi:10.1029/2012ja017943.

Omura, Y., and Q. Zhao (2013), Relativistic electron microbursts due to nonlinear pitch angle scattering by EMIC triggered emissions, *J. Geophys. Res.*, *118*(8), 5008–5020, doi:10.1002/jgra.50477.

Press, W. H., B. P. Flannery, S. A. Teukolsky, and W. T. Vetterling (1986), *Numerical Recipes*, Cambridge Univ. Press, New York.

Ronnmark, K. (1982), Waves in homogeneous, anisotropic, multicomponent plasmas, *Tech. Rep. Kiruna Geophys. Inst. Rep. 179, 56 pp.*, Swedish Institute of Space Physics, Univ. of Umea, Sweden.

Ronnmark, K. (1983), Computation of the dielectric tensor of a maxwellian plasma, *Plasma Physics and Controlled Fusion*, *25*(6).

Shprits, Y. Y., D. A. Subbotin, N. P. Meredith, and S. R. Elkington (2008), Review of modeling of losses and sources of relativistic electrons in the outer radiation belt. ii: Local acceleration and loss, *J. Atmos. Sol.-Terr. Phys.*, *70*(14), 1694–1713, doi:10.1016/j.jastp.2008.06.014.

Summers, D., B. Ni, and N. P. Meredith (2007), Timescales for radiation belt electron acceleration and loss due to resonant wave-particle interactions: 1. theory, *J. Geophys. Res.*, *112*(A4), doi:10.1029/2006JA011801.